

pubs.acs.org/ac Article

# Time-Domain Photothermal AFM Spectroscopy via Femtosecond Pulse Shaping

Miriam Bohlmann Kunz, Yulia Podorova, Zachary T. Armstrong, and Martin T. Zanni\*



Cite This: Anal. Chem. 2022, 94, 12374-12382



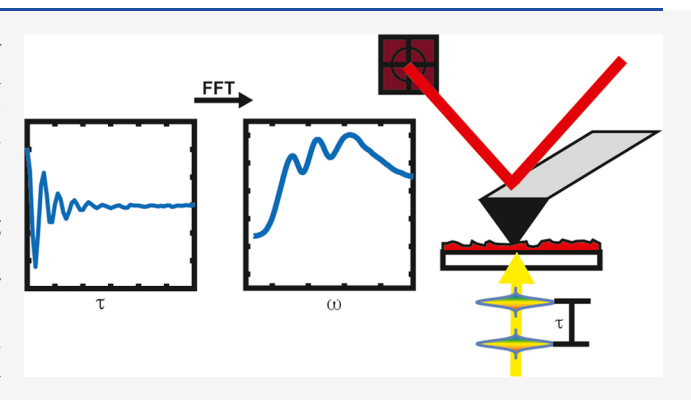
**ACCESS** I

Metrics & More

Article Recommendations

Supporting Information

ABSTRACT: A time-domain version of photothermal microscopy using an atomic force microscope (AFM) is reported, which we call Fourier transform photothermal (FTPT) spectroscopy, where the delay between two laser pulses is varied and the Fourier transform is computed. An acousto-optic modulator-based pulse shaper sets the delay and phases of the pulses shot-to-shot at 100 kHz, enabling background subtraction and data collection in the rotating frame. The pulse shaper is also used to flatten the pulse spectrum, thereby eliminating the need for normalization by the laser spectrum. We demonstrate the method on 6,13-bis-(triisopropylsilylethynyl)pentacene (TIPS-Pn) microcrystals and Mn-phthalocyanine islands, confirming subdiffraction spatial resolution, and providing new spectroscopic insights likely linked to structural defects in the crystals.



## **■ INTRODUCTION**

Some of the most interesting and least well-understood variation of material properties occurs at subdiffraction length scales, such as the structural variation between grains in a thin film, <sup>1–3</sup> the behavior of an isolated nanoparticle, <sup>4,5</sup> or edge effects in a single crystal. <sup>6–8</sup> These regions are often of interest because the variation at grain boundaries and the edge effects in single crystals can perturb the electronic structure significantly resulting in increased or decreased charge carrier generation or mobility when used in photovoltaic devices, <sup>9,10</sup> whereas nanoparticles have shown to be catalysts for various reactions, which is strongly affected by the electronic structure. <sup>11,12</sup> Ideally, the spectroscopic information of each region would be measured separately, but in typical far-field microscopies where the spatial resolution is limited by the diffraction of light, the responses from each of these regions are convoluted with one another.

There are various methods of subdiffraction limit imaging, including electron microscopy, fluorescence techniques such as stochastic optical reconstruction microscopy. and reversible saturable optical fluorescence transitions (RESOLFT) techniques, <sup>14–16</sup> as well as scanning probe techniques such as scanning tunneling microscopy (STM)<sup>17</sup> and atomic force microscopy (AFM). Scanning probe microscopies in combination with light-matter interactions have been used to measure spectroscopic information with subdiffraction limit spatial resolution. Two of these most common scanning probe spectroscopic techniques are scanning scattering near-field optical microscopy (s-SNOM)<sup>21</sup> and AFM infrared spectroscopy (AFM-IR). AFM-IR is closely related to the technique presented here. AFM-IR is a photothermal method, in which a

tunable-wavelength laser pulse illuminates the sample, and if the light is absorbed, the photon energy ultimately becomes thermal energy, leading to an increase in temperature, a thermal expansion, and thereby an upward force on the AFM cantilever that is in contact with the sample, causing it to oscillate. The amplitude of this oscillation is proportional to the amount of light absorbed. The AFM-IR principle has also been used to measure visible light absorption. Previous implementations of AFM-detected spectroscopy have measured the degradation of MAPbI<sub>3</sub> films, amped domains in metal—organic frameworks with mixed linkers, and chemically mapped cancer cells. For more details on previous AFM-detected spectroscopies and nanoscale imaging, we direct the reader to recent reviews on the topic.

Here, we present the first implementation of Fourier transform photothermal (FTPT) spectroscopy. To date, photothermal AFM detection has almost exclusively been implemented in the frequency domain, where the cantilever response is measured as a function of the laser frequency. Our method operates in the time domain, where instead of scanning the frequency of the excitation pulse, we scan the time delay between two laser pulses to measure a free-induction decay

Received: May 1, 2022 Accepted: August 12, 2022 Published: August 30, 2022





(FID). We then Fourier transform this FID to retrieve the absorption spectrum. The approach is analogous to timedomain methods using a Michelson interferometer in scatteringtype scanning near-field optical microscopy (s-SNOM) measurements,<sup>32</sup> and with incoherent light and a Michelson interferometer using synchrotron broadband-IR sources, 33,34 albeit the pulse shaper used here enables new modes of data collection not previously possible, such as data collection utilizing phase cycling, a rotating frame, time-delay reordering, and the creation of a flat laser spectrum. The method presented here uses an ultrafast visible supercontinuum created simply by pumping a bulk material, 8 mm YAG, with less than 4  $\mu$ J of 1040 nm fundamental power. The advantage of the presented method versus previous time-domain methods in the IR is that it can be done with a commercially available light source. In addition, the use of coherent femtosecond pulses gives the method potential for being extended to a multidimensional method, with both high temporal and spatial resolution, which would not be possible with nanosecond pulses. We demonstrate the capabilities here, explain the theory behind the approach, and detail the technical factor necessary to implement the technique.

#### EXPERIMENTAL SECTION

Our Fourier transform photothermal experiment adapts a previously described 2D white light microscope,  $^{35}$  as shown in Figure 1. Briefly, 5  $\mu$ J of a 100 kHz Yb amplifier centered at 1040

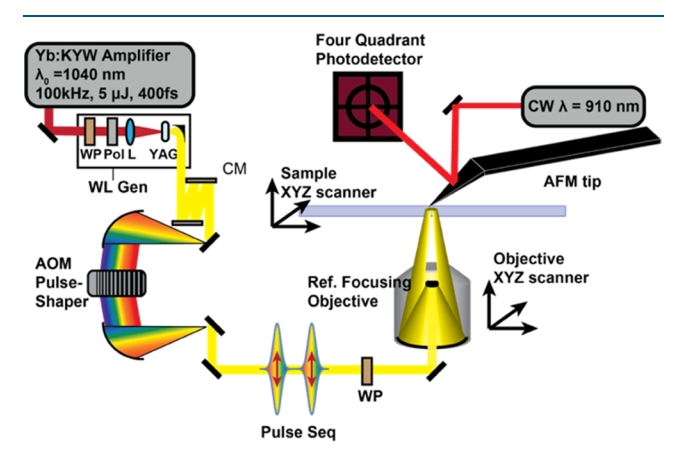


Figure 1. Experimental design and layout. WP: waveplate, Pol: polarizer, L: lens, CM: chirped mirrors.

nm pumps an 8 mm YAG crystal to create a supercontinuum. This supercontinuum is then compressed using broadband chirped mirrors (Layertec) and phase compensation in an acousto-optic modulator pulse shaper.<sup>36</sup> The spectrum of the shaped light is measured by directing the light immediately after the pulse shaper into a spectrometer, where it is dispersed by a grating and focused onto a CCD line scan camera (e2V AviivA EM4). The spectral range of the white light is 520-800 nm, although this is mostly windowed to 540-720 nm, as described in more detail below. The delay time possible with an AOM pulse shaper is only limited by a maximum possible delay, which is in the order of picoseconds and is much greater than the final delay needed for electronic transitions. The size of the delay time steps determines the maximum frequency (minimum wavelength) resolvable, and the final delay time determines the spectral resolution, which is 260 cm<sup>-1</sup> for all spectra reported here. The deflected light from the pulse shaper is directed into an AFM (Molecular Vista) from below the sample using a reflective

objective, which focuses the beam to a spot size of approximately one micrometer. An achromatic half waveplate rotates the polarization of the light relative to the sample in the microscope. The beam is aligned beneath the AFM tip (HQ:NSC14/Pt MikroMasch) by scanning the position of the reflective objective while the AFM tip is in contact with the sample. The AFM probe used has a moderate force constant of 5 N/m, a diameter of less than 30 nm, and a free resonance near 160 kHz. The AFM probe takes  $60\,\mu s$  to return to equilibrium after being excited by sample expansion. The position of the beam relative to the AFM tip is set to maximize the deflection of the continuous wave laser reflecting off the back of the AFM probe.

An optically detected linear absorption spectrum on a single 6,13-bis(triisopropylsilylethynyl)pentacene (TIPS-Pn) crystal was measured on the CCD line scan camera using the FTPT microscope. After the sample, the light was recollimated in a transmissive objective, coupled into an optical fiber, and directed into a spectrometer. The light used in all of the microscope and FTPT experiments was linearly polarized. For a photothermal imaging experiment, a single supercontinuum pulse is used. To scan the position, the objective and AFM positions are fixed, and the sample stage is translated. The topography and photothermal information are collected simultaneously. The signal collected in a photothermal image represents the total absorption at all wavelengths for a given position on the sample, and the amount of time averaged per pixel is approximately 50 ms.

Films of 6,13-bis(triisopropylsilylethynyl)pentacene (TIPS-Pn) microcrystals were grown by drop casting 100  $\mu L$  of 5 mg/mL TIPS-Pn in toluene onto a microscope slide held at 50 °C to create crystals that were 10–20  $\mu m$  in width, 100–300 nm in height, and several millimeters in length. The bulk absorption spectrum of the TIPS-Pn microcrystal film was measured using a standard UV–vis spectrometer (Cary UV–vis Spectrophotometer). Islands of Mn-pthalocyanine (MnPc) were made by drop casting a filtered saturated solution of MnPc in DMSO (<0.5 mg/mL) onto a glass slide held at room temperature for 72 h resulting in a featureless amorphous film. This film was solvent annealed in chloroform vapor for 12 h, resulting in small islands of crystalline MnPc.

**Theory of FTPT Spectroscopy.** In this section, we cover some of the mathematical principles used to collect FTPT spectra. The pulse shaper is used to generate two femtosecond pulses, as depicted in Figure 2a,b, separated by a time delay  $t = \tau_1$  $-\tau_2$ . Each pulse has a phase,  $\varphi_n$ . We want to measure the heat caused by the pair of pulses, but each individual pulse also heats the sample, creating a background. Shown in Figure 2c are the Feynman diagrams for the background and desired signal. In this formalism, heat is created when the pulses end in an excited state population,  $|e\rangle\langle e|$ , that subsequently relaxes to the ground state as the sample thermalizes. Thermalization causes a temperature rise,  $\Delta T^{(n)}$ , and an expansion of the sample. To create a population state, the sample must interact twice with the pulse electric fields, E. For the two background pathways (i) and (ii), the two electric field interactions will occur within the width of a single pulse, centered at either  $\tau_1$  or  $\tau_2$ , and give temperature rises  $\Delta T^{(1)}$  and  $\Delta T^{(2)}$ , respectively. The signal pathway (iii) is by pulse one,  $E_1$ , and pulse two,  $E_2$ , each interacting once with the sample at  $\tau_1$  and  $\tau_2$ , respectively, thereby spaced by  $t = \tau_2 - \tau_1$ , which we refer to as the delay time. This pathway also ends in an excited population and decays back to the ground state through the same nonradiative mechanism as pathways (i) and (ii), resulting in another increase in temperature,  $\Delta T^{(12)}$ .

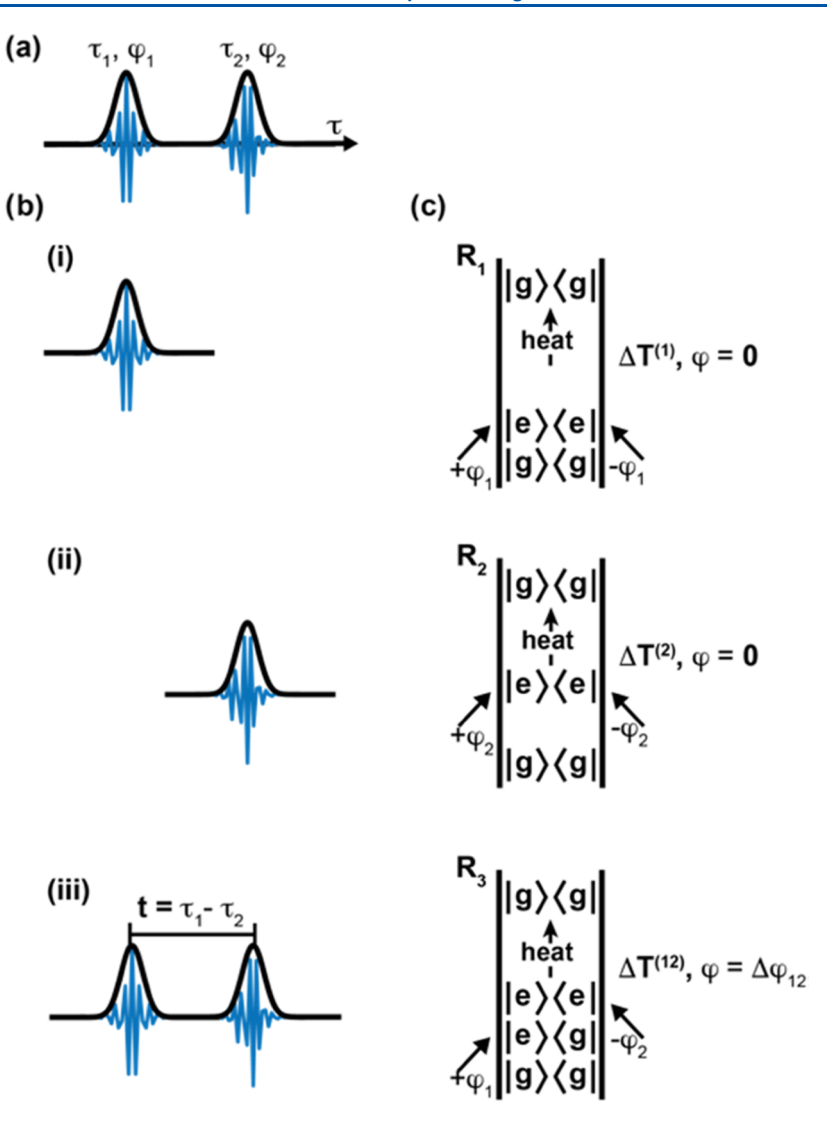


**Figure 2.** Formalism behind FTPT measurements. Each pulse pair (a), with a delay time, *t*, has three possible pathways that lead to absorption in the sample (b, c). Feynman diagrams (i) and (ii) show pathways where pulse one and pulse two, respectively, each interact with the sample twice. Feynman diagram (iii) illustrates the scenario where each pulse interacts with the sample once, and therefore it is dependent both on the phase and delay time of the pulse pair.

The response functions,  $R_n$ , for each Feynman pathway are given in eq 1.

$$R_1 \propto i\mu_{\rm ge}^2$$

$$R_2 \propto i\mu_{\rm ge}^2$$

$$R_3 \propto i\mu_{\rm ge}^2 e^{-i\omega_{\rm ge}(\tau_1 - \tau_2)} e^{-(\tau_1 - \tau_2)/T_2} = i\mu_{\rm ge}^2 e^{-it\omega_{\rm ge}} e^{-t/T_2}$$
(1)

where  $\omega_{\rm ge}$  is the resonant frequency for the transition from the ground to an excited state,  $\mu_{\rm ge}$  is the transition dipole moment, and  $T_2$  is the homogeneous dephasing, which takes into account population relaxation and fluctuations of the environment.<sup>37</sup> The notation follows that of Hamm and Zanni (Cambridge Univ Press).<sup>37</sup> From these three expressions for the response functions, it is clear that  $R_1$  and  $R_2$  are not dependent on the time between the two pulses, but the real value of  $R_3$  oscillates as a function of the delay time. In other words, because pathway (iii) depends on t, the temperature in the sample is modulated by the delay time.

The signal is given by the convolution of the response functions with the electric fields of the laser pulses

$$S(\tau) \propto E(\tau) \otimes R(\tau)$$
 
$$E(\tau) \propto A(\tau)e^{\pm i\omega_c\tau \mp i\varphi \mp i\vec{k} \cdot \vec{\tau}}$$
 (2)

where  $\omega_c$  is the carrier frequency of the electric field, which in the limit of  $\delta$ -function envelopes becomes

$$S(\tau) \propto iE_1(\tau_1)E_1^*(\tau_1)R_1 + iE_2(\tau_2)E_2^*(\tau_2)R_2 + iE_1(\tau_1)E_2^*(\tau_2)R_3$$
(3)

which gives

$$S(t) \propto I_{\mu} \mu_{ge}^{2} + I_{2} \mu_{ge}^{2} + I_{12} e^{it(\omega_{c} - \omega_{ge})} e^{-i\Delta \phi_{12}} \mu_{ge}^{2}$$

$$\propto \Delta T^{(1)} + \Delta T^{(2)} + \Delta T^{(12)}(t)$$
(4)

Where  $\Delta \varphi_{12}$  is the relative phase between  $E_1$  and  $E_2$ , and  $I_n$  is the intensity of the laser pulse pair. The intensity,  $I_n$ , should be the same for pulse one and pulse two and the interaction with both

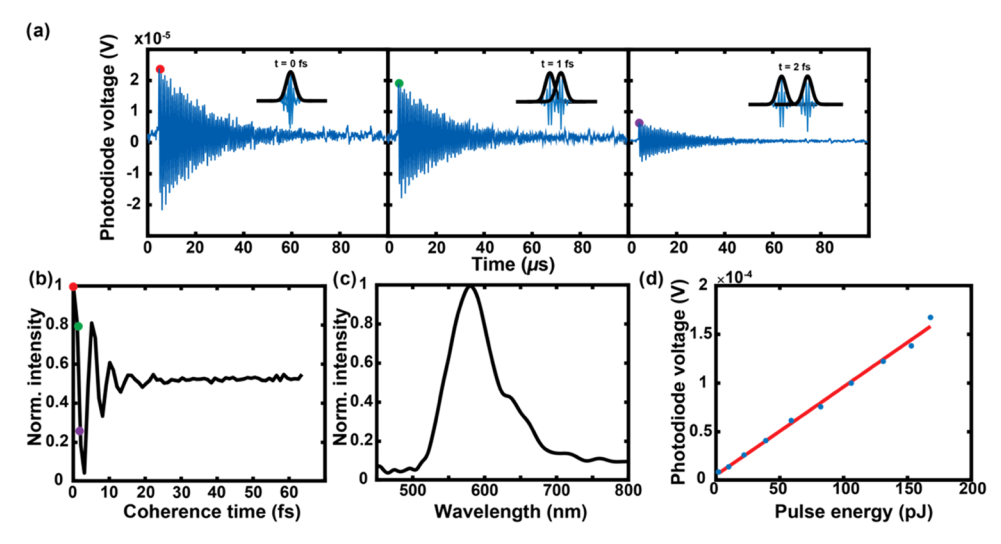


**Figure 3.** Linear response of AFM photothermal detection. Panel (a) shows examples of the magnitude of the AFM oscillations for different delay times and how the maximum amplitude for each pulse pair (red, green, and purple dots) corresponds to the respective points in the FID of TIPS-Pn (b). The FID is then Fourier transformed to obtain the absorption spectrum (c). Panel (d) demonstrates that the AFM photodiode voltage is linear with the intensity of the light.

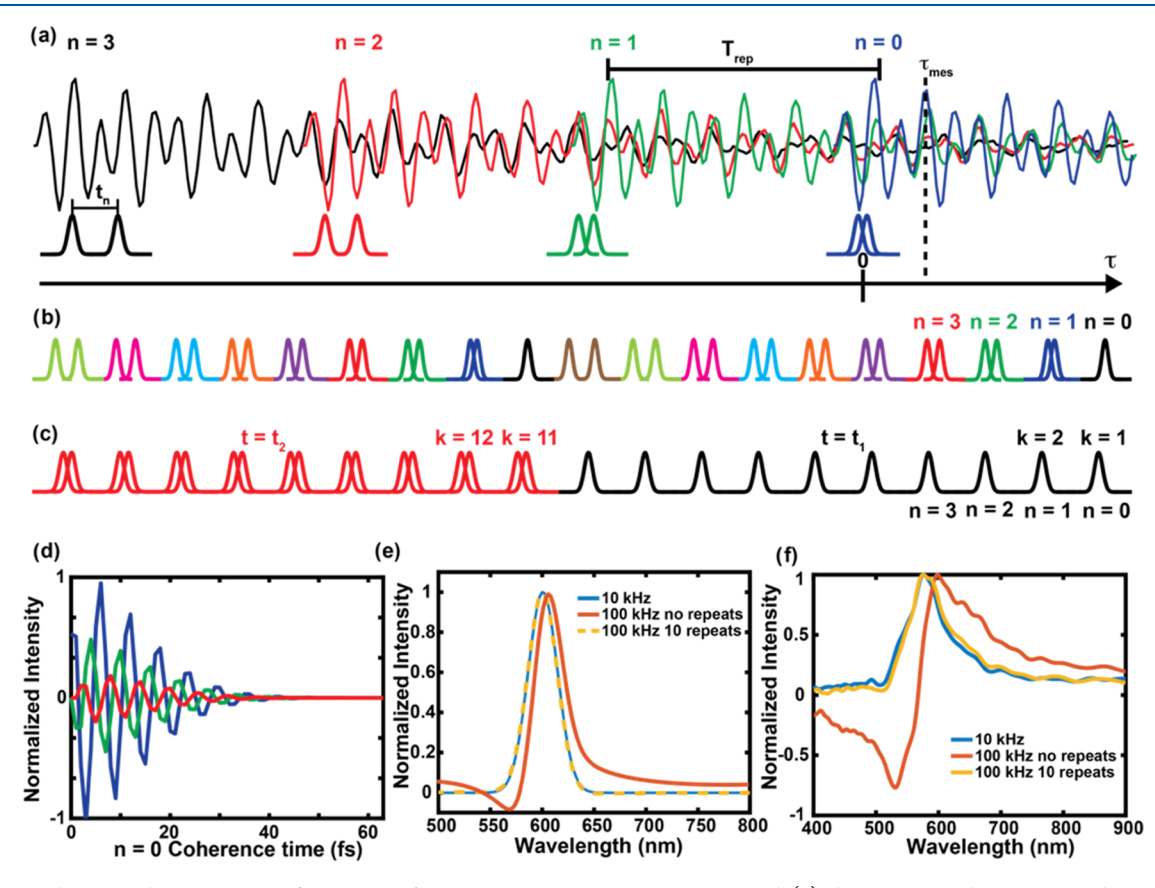


**Figure 4.** Simulation and experiments of AFM interference on FTPT measurements. Panel (a) demonstrates the AFM cantilever oscillations originating from four different pulse pairs, n = 0-3, with corresponding delay times,  $t_n$ . The time between the pulses is shown as  $T_{\text{rep}}$ , and the time the AFM oscillation is measured as  $\tau_{\text{mes}}$ . The pulse sequences are considered, the first (b) has a different delay time for every pulse pair. The second pulse sequence (c) repeats each delay time for 10 pulses so that pulses k = 1-10 have  $t = t_1$  and pulses k = 11-20 have  $t = t_2$ . The contribution to the time-domain signal,  $S(t_0)$ , from pulse pairs t = 0-2 is shown in panel (d), with blue, green, and red corresponding to pulse pairs t = 0, t = 0, and t = 0, and t = 0, t = 0

pulses. Equation 4 is experimentally measured and plotted as the FID. The phase,  $\Delta \varphi_{12}$ , can be changed as a function of the delay time to operate in a rotating frame, thereby lowering the Nyquist

frequency.<sup>38</sup> The use of an ultrafast pulse shaper in these experiments allows for a rotating frame of 11,000 cm<sup>-1</sup> to be used for all measurements presented here. In addition, a

Gaussian window function with a width of 40 fs was used to minimize the noise for delay times after the signal had decayed to a level below the noise threshold.

In our experiment, photons are not directly measured. Instead, the heat generated by the absorbed photon causes an expansion of the sample, which the AFM detects. The thermal expansion is also dependent on the thermal expansion coefficients and thermal diffusivity. Experimentally, the contribution from each pathway will result in an increase in temperature,  $\Delta T^{(1)}$ ,  $\Delta T^{(2)}$ , and  $\Delta T^{(12)}$ , all causing an expansion.  $\Delta T^{(1)}$  and  $\Delta T^{(2)}$  are independent of the delay time. Whereas  $\Delta T^{(12)}$  will depend on the delay time, creating an oscillation. Previous theoretical work has shown that the maximum deflection of the AFM cantilever due to the expansion of the sample is linearly proportional to the amount of light absorbed, the Fourier transform gives the desired spectrum.

$$S(\omega) = \int_0^\infty S(t)e^{i\omega t}dt \tag{5}$$

### ■ RESULTS AND DISCUSSION

Shown in Figure 3 is the application of FTPT to microcrystals of TIPS-Pn. The absorption spectrum of TIPS-Pn is discussed in more detail below, but for this section, the nature of the sample is not important. Figure 3a shows the AFM response for three different time delays, t. After each pair of pulses, the AFM probe is deflected, followed by oscillations of the probe, which last 60  $\mu$ s. The intensity and phase of the AFM oscillations depend on the phases and delay time of the pulses, according to eq 4. To measure an FID of the response, the maximum value of the AFM oscillations for each laser shot is plotted as a function of the delay time, t, as illustrated in Figure 3b. Figure 3c shows the Fourier transform of the FID to retrieve the spectrum. Each point in the FID is measured 10 times for a single FID, as discussed in more detail below, which results in each FID taking 6.4 ms to measure. However, due to relatively low pulse energies and the repetition rate of the laser not being tunable to the cantilever resonance, tens of thousands of averages are used for a single spectrum, which takes between 2 and 5 min, depending on the sample.

For eqs 4 and 5 to hold, the AFM amplitude must be linearly proportional to the amount of light absorbed by the sample. Figure 3d plots the maximum AFM photodiode voltage as a function of pulse energies, showing a linear response. Although nonlinear signals are possible and measurable in higher-order experiments, such as transient absorption and 2D white light spectroscopy, these nonlinear signals are 3 orders of magnitude less than the linear signals. In addition, we do not observe the nonlinear thermal expansion effect,<sup>39</sup> which would result in a slope of the FID but is not present in the FTPT data.

**Effect of Laser Repetition Rate on AFM Response.** As mentioned above, the AFM cantilever used in these experiments takes approximately  $60 \, \mu s$  to return to rest. At a repetition rate of  $100 \, kHz$ , the time between laser pulses is  $10 \, \mu s$ . Thus, the AFM deflection is caused not only by the immediately preceding pair of pulses but also by the prior pairs of pulses, each to a lesser degree. In this section, we show the effects of this fact and a means for minimizing its deleterious effects.

Figure 4a illustrates the issue by plotting the oscillations of the AFM cantilever for four consecutive pulse pairs, n = 0-3. For an FTPT measurement, there is a fixed time that is interrogated every  $10 \ \mu s$ , or once every new pulse pair. This is referred to as the measurement time,  $\tau_{\rm mest}$  and is shown as the dashed black

line in Figure 4a. The first pulse pair, n=0, is shown in blue. The blue pulse pair,  $t_0$ , contributes a discrete amplitude to the AFM oscillations at  $\tau_{\rm mes}$  that is dependent on the signal,  $S(t_0)$ , the time constant for the AFM oscillations decaying,  $\tau_{\rm AFM}$ , and the mechanical resonances of the AFM cantilever,  $\omega_{\rm m}$ . The contribution to the time-domain signal is shown in Figure 4d. The pulse pair in green, n=1, also contributes a discrete amplitude to the AFM oscillations at  $\tau_{\rm mes}$ , which is dependent on  $S(t_1)$ . For a given value of  $S(t_n)$ , the contribution from n=1 is less than the contribution at n=0 because n=1 is farther away in time from  $\tau_{\rm mes}$ , so the AFM response created by n=1 will have decayed a greater amount. The effect of the AFM oscillations decaying is even more pronounced for pulses farther removed from  $\tau_{\rm mes}$ .

We can express the measured signal as the following

$$S_{\text{tot}}(t) = \sum_{k} \sum_{n} e^{-(\tau_{\text{mes}} + nT_{\text{rep}})/\tau_{\text{AFM}}} e^{i\omega_{m}(\tau_{\text{mes}} + nT_{\text{rep}})} \cdot S(t_{k+n})$$
(6)

where k is the index for the number of times each delay time is repeated, n is the number of pulses before  $\tau_{\text{mes}}$ , as illustrated in Figure 4, and  $T_{rep}$  is the time between laser pulses. Using this expression, we simulated the FTPT measurement for three different conditions. Situation one is when  $T_{\text{rep}} = 100 \,\mu\text{s}$  (10 kHz repetition rate) and k = 1 so that  $T_{rep}$  is longer than the AFM oscillations and so the AFM only reads out the thermal response of the immediately preceding pair of pulses. Situation two is when  $T_{\text{rep}} = 10 \,\mu\text{s}$  (100 kHz), k = 1, which is illustrated by the pulse sequence in Figure 4b, where multiple pulses contribute to the AFM readout. Situation three is when  $T_{\text{rep}} = 10 \ \mu\text{s}$  (100 kHz), k = 10, which is illustrated by the pulse sequence in Figure 4c. In situation three, only pulse pairs with two different delay times (Figure 4c black and red) will contribute to the signal at a given  $\tau_{\rm mes}.$  For the simulations, we used a Gaussian distribution of frequencies centered at 600 nm with a width of 40 nm. The inverse Fourier transform was computed to obtain the timedomain response.

The simulations of situations one, two, and three are plotted in Figure 4e in blue, orange, and yellow, respectively. The simulation of situation one results in the same Gaussian distribution that was input into the simulation, as there is no interference in situation one. The simulation of situation two illustrates that at 100 kHz, the AFM cantilever does not have time to return to equilibrium before the next pulse pair. As a result, the temperature rise from prior pulse pairs contributes to the signal with intensity and phase set by the oscillation frequency of the AFM ringdown and the repetition rate of the laser. The multiple signals interfere, and for situation two, where the delay time for every pulse pair is different, this results in a distorted spectrum. For situation three, where all of the interfering AFM oscillations originate from only two delay times, the simulated spectrum almost perfectly recreates the spectrum for situation one, where there was no interference.

The three simulated situations were also repeated experimentally, shown in Figure 4f. Just as shown in the simulation, the experiments at 10 kHz and 100 kHz with repeating delay times show no distortion (Figure 4f, blue and yellow, respectively), but the experiment at 100 kHz with no repeating delay times does show a distorted spectrum (Figure 4f orange).

An alternative way to address the complication of interfering AFM oscillations is to reduce the laser repetition rate, as we demonstrated in the simulation and experiment (Figure 4d,e blue). However, it is preferable to operate at the maximum repetition rate of the pulse shaper, which is 100–200 kHz, to

decrease the amount of time needed to average. In what follows, we use situation three, a repetition rate of 100 kHz and delay times repeated for 10 consecutive laser shots, for all of the reported spectra.

FTPT of TIPS-Pn Using a Square Spectral Bandwidth for Auto-Normalization. In absorption spectroscopy, the optical density is typically reported by measuring the spectrum with (foreground) and without (background) the sample and dividing. This process deconvolutes the spectral variations in the intensity of the light source from the molecular information. Making an analogous background measurement with photothermal AFM is more difficult because removing the sample eliminates any signal; a control sample is needed to create an expansion with a known thermal response. Moreover, it is technically difficult to exchange samples on an AFM while maintaining the precise alignment of the laser and the AFM probe. Indeed, in Figures 2 and 3 above, we did not present optical density and so the spectra were strongly modulated by the spectrum of the laser pulse.

Pulse shaping provides an alternative method. The pulse shaper is used to modify the amplitude of the laser spectrum such that the laser spectrum has the same intensity at every wavelength within a defined window and is zero for all other wavelengths, creating a flat spectrum, such as the square spectrum shown in Figure 5a (orange), created by shaping the laser pulse spectrum.

To illustrate the improvement of using a flat spectrum versus the full laser spectrum, Figure 5b in purple shows the FTPT spectrum on a TIPS-Pn microcrystal taken with the full laser spectrum and then divided by the relative laser intensity at each wavelength (Figure 5a, blue). There are two peaks at 580 and 650 nm, but the spectrum at the edges of the laser spectrum is not physical due to division by small numbers. Also shown in Figure 5b (red) is the FTPT spectrum from the same spot, but with a square laser spectrum so that no normalization is required. With the square laser spectrum, the same two peaks at 580 and 650 nm are evident, as well as an additional peak at 700 nm that is not discernable in the normalized FTPT spectrum. The data presented in the remainder of the manuscript are collected using a square pulse spectrum.

TIPS-Pn Spectrum via FTPT. The spectroscopic capabilities of FTPT are demonstrated on TIPS-Pn microcrystals (Figure 6). In Figure 6a is plotted a bulk absorption spectrum of TIPS-Pn microcrystals (orange solid), an optically detected microscope spectrum from a TIPS-Pn microcrystal (orange dashed), and an FTPT spectrum from the same location as the optically detected spectrum (blue). The bulk absorption spectrum resembles those previously reported by our research group and in the literature.<sup>6</sup> The main spectroscopic feature is a vibronic progression with three peaks, each centered at 700, 650, and 590 nm. There is also broad continuous absorption at energies above the vibronic progression. All three spectra in Figure 6a have the expected three vibronic peaks at the same wavelengths. The intensity of the vibronic peaks relative to the continuous absorption is greater in the microscope and FTPT spectra versus the bulk absorption spectrum. This is likely due to the bulk spectrum being measured with unpolarized light, whereas the microscope and FTPT spectra were measured with linearly polarized light. We note that in the microcrystals, the TIPS-Pn molecules are oriented such that the transition dipole of the S<sub>1,n</sub> states are aligned roughly along the short axis of the crystal.6

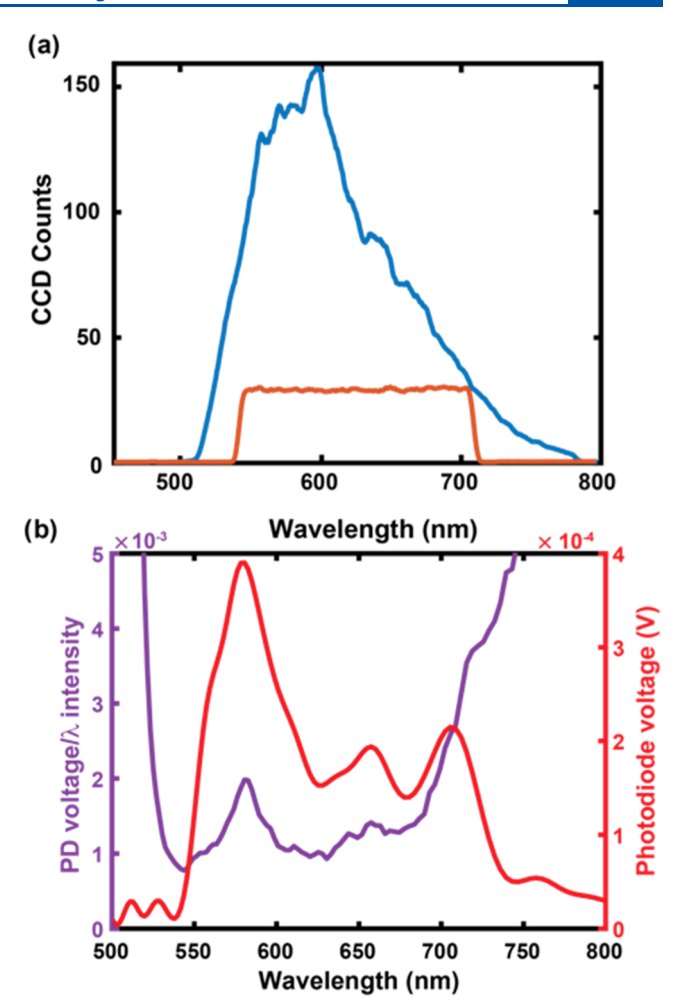


**Figure 5.** Pulse shaping to flatten the laser spectrum. The spectrum of the laser pulse (a) is shown in blue. The AOM pulse shaper is used to modify the amplitude of the spectrum at each wavelength to create a square laser spectrum, shown in orange. FTPT spectra (b) on a TIPS-Pn microcrystal were measured using the full laser pulse and then normalized for the intensity of the light at each wavelength (purple) and with a square laser spectrum (red).

Figure 6c shows the FTPT spectra at three different spots on a TIPS-Pn microcrystal (Figure 6b). Spot one (yellow) is off the crystal, and only small amounts of TIPS-Pn are measured, hardly above the noise of the measurement. Spots two and three are from near the edge and the center of the crystal, respectively. We note that the relative intensity of the 650 nm peak at the edge of the crystal is much smaller than the center of the crystal. We have previously reported that the structure of TIPS-Pn at the edges of crystals has defects. We tentatively assign this change in intensity to the effects of those defects. <sup>6,40</sup>

Simultaneous Photothermal and Topographical Imaging. Mn-phthalocyanine (MnPc) islands were used to test the spatial resolution of the photothermal microscope. When deposited as described in the methods, MnPc forms islands with diameters on the order of hundreds of nanometers, and heights of 70–120 nm, as shown in the topography image in Figure 7a. The islands formed are pancake in shape, with the diameter exceeding the height of the islands. The photothermal absorption from the MnPc film (Figure 7b) was collected simultaneously with the topography. The step size for the images in Figure 7 is 20 nm. As described in the Experimental Section, the photothermal image shows the AFM deflection for an

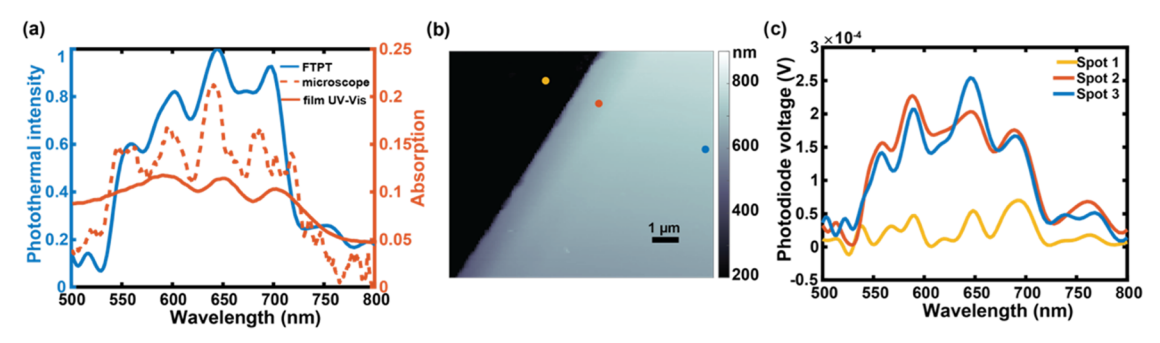


**Figure 6.** TIPS-Pn spectra measured via FTPT. (a) The bulk spectrum of TIPS-Pn (solid orange) agrees well with the optically detected microscope spectrum (dashed orange) and FTPT spectrum (blue). Panel (b) shows the topography at the edge of a TIPS-Pn microcrystal. FTPT spectra were measured at three different spots (c) corresponding to the locations of the same colored dots in (b).

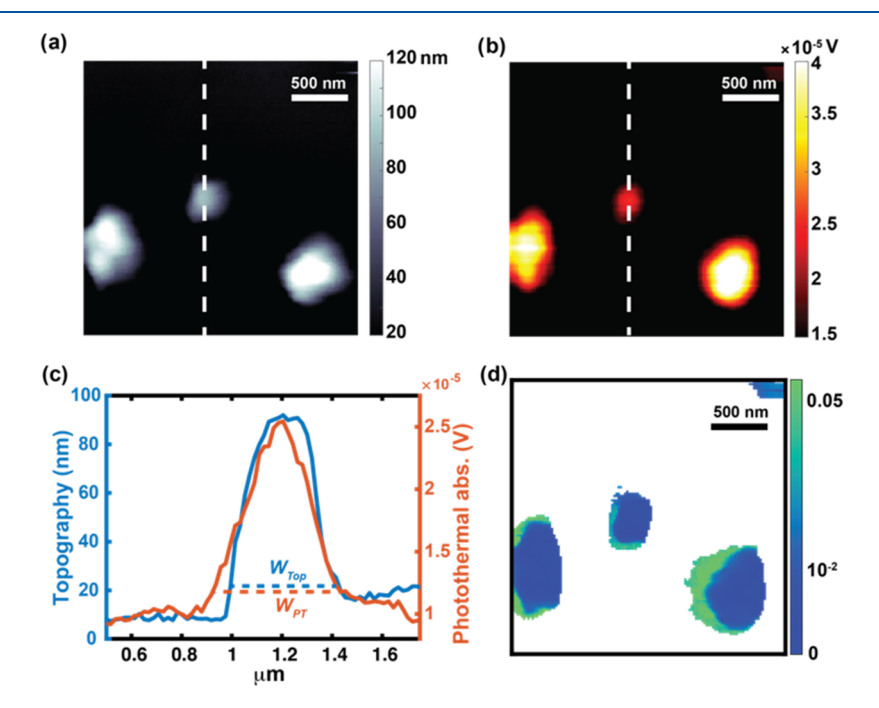


Figure 7. Photothermal imaging of MnPc islands. The topography and photothermal absorption images of MnPc islands are shown in panels (a) and (b), respectively. Cross-sections through the topography and photothermal absorption (c) demonstrate the subdiffraction limit spatial resolution of AFM-detected photothermal microscopy. Panel (d) plots the photothermal absorption divided by the height for all pixels with at least 25% of the maximum photothermal signal, plotted on a log scale.

unmodified laser pulse. It is not feasible to measure a spectrum at every pixel, as each spectrum takes 2-5 min, and there are over 65,000 pixels in a typical image. However, it is possible to use the pulse shaper to window the pulse to a specific spectral region and measure the photothermal expansion for that window (Figure S1). The photothermal image shows absorption from all three islands, even though the diameter of the islands can be as small as 200 nm, which is near the diffraction limit of light. To determine the spatial resolution of the photothermal imaging, we have plotted a cross-section through the topography and photothermal images (Figure 7c) and determined the full width at 10% of the maximum for the topography,  $W_{\text{Top}}$ , and the full width at 10% of the maximum for the photothermal absorption,  $W_{\rm PT}$ , and the difference between the two widths was calculated.<sup>26</sup> The average difference in the widths for 40 different cross-sections, 20 vertical and 20 horizontal, was 49  $\pm$ 36 nm. Additional cross-sections are shown in Figure S2. The diffraction limit of the shortest wavelength of light in our laser spectrum, 550 nm, is 200 nm. Thus, the spatial resolution of the

AFM-detected photothermal image is significantly below the diffraction limit.

Figure 7d shows the normalized photothermal absorption divided by the topography for all pixels with at least 25% of the maximum photothermal intensity. The absorption relative to the height of the islands is larger on one side of the islands, regardless of the direction the AFM was scanned, indicating this was not an artifact due to poor tracking of the AFM tip. A possible physical origin for the increased relative absorption on one side of the islands is that the crystals grow from one side as the solvent evaporates. We have previously measured crystallin disorder that depends on crystal growth.

## CONCLUSIONS

Fourier transform photothermal spectroscopy is a time-domain method for measuring spectroscopic information with sub-diffraction limit spatial resolution. Photothermal detection is a well-established method used in frequency domain AFM-IR and visible AFM experiments, <sup>26,41</sup> but operation in the time domain allows for the use of ultrafast, broadband pulses. Utilizing a pulse

shaper also enables pulse sequences that utilize phase cycling, a rotating frame, data collection with flat-intensity pulses, and arbitrary ordering of pulse delays for optimizing data collection to the repetition rate of the laser and the AFM decay time. We generate linear spectra, but the Potma group has performed AFM-detected pump-probe experiments. Pump-probe and 2D optical spectroscopies are both third-order experiments. Thus, it should be possible to extend the FTPT measurements here to multidimensional spectroscopy using the pulse shaper to generate more sophisticated pulse trains.

#### ASSOCIATED CONTENT

## **Solution** Supporting Information

The Supporting Information is available free of charge at https://pubs.acs.org/doi/10.1021/acs.analchem.2c01920.

(SI) further explanation of interfering AFM oscillations; (SII) photothermal imaging with spectrally windowed pulses; and (SIII) imaging cross-sections through Mn-phthalocyanine nanoislands (PDF)

## AUTHOR INFORMATION

#### **Corresponding Author**

Martin T. Zanni — Department of Chemistry, University of Wisconsin-Madison, Madison, Wisconsin 53706, United States; orcid.org/0000-0001-7191-9768; Email: zanni@chem.wisc.edu

#### **Authors**

Miriam Bohlmann Kunz — Department of Chemistry, University of Wisconsin-Madison, Madison, Wisconsin 53706, United States; Occid.org/0000-0002-7852-159X

Yulia Podorova — Department of Chemistry, University of Wisconsin-Madison, Madison, Wisconsin 53706, United States

Zachary T. Armstrong — Department of Chemistry, University of Wisconsin-Madison, Madison, Wisconsin 53706, United States; orcid.org/0000-0002-1207-6171

Complete contact information is available at: https://pubs.acs.org/10.1021/acs.analchem.2c01920

#### Notes

The authors declare the following competing financial interest(s): M.T.Z. is a co-owner of PhaseTech Spectroscopy, which sells ultrafast pulse shapers and multidimensional spectrometers similar to the equipment utilized here.

## ACKNOWLEDGMENTS

The authors acknowledge funding from the NSF for supporting the TIPS pentacene experiments reported here via grant CHE-1954700. The AFOSR funded the equipment purchases and the initial pulse sequence development via grant FA9550-19-1-0093. This material is based upon work supported by the National Science Foundation Graduate Research Fellowship Program (M.B.K.) under Grant No. DGE-1747503. Any opinions, findings, conclusions, or recommendations expressed in this material are those of the authors and do not necessarily reflect the views of the National Science Foundation.

## REFERENCES

- (1) Major, J. D. Semicond. Sci. Technol. 2016, 31, No. 093001.
- (2) Seager, C. H. Annu. Rev. Mater. Sci. 1985, 15, 271-302.

- (3) Zong, Y.; Zhou, Y.; Zhang, Y.; Li, Z.; Zhang, L.; Ju, M.-G.; Chen, M.; Pang, S.; Zeng, X. C.; Padture, N. P. Chem 2018, 4, 1404—1415.
- (4) Xie, T.; Jing, C.; Long, Y.-T. Analyst 2017, 142, 409-420.
- (5) Sambur, J. B.; Chen, P. Annu. Rev. Phys. Chem. 2014, 65, 395–422.
- (6) Jones, A. C.; Kearns, N. M.; Ho, J.-J.; Flach, J. T.; Zanni, M. T. *Nat. Chem.* **2019**, 1–8.
- (7) Hickey, C. L.; Grumstrup, E. M. Nano Lett. 2020, 20, 5050-5056.
- (8) Bender, J. A.; Raulerson, E. K.; Li, X.; Goldzak, T.; Xia, P.; Van Voorhis, T.; Tang, M. L.; Roberts, S. T. *J. Am. Chem. Soc.* **2018**, *140*, 7543–7553.
- (9) Tavakoli, M. M.; Bi, D.; Pan, L.; Hagfeldt, A.; Zakeeruddin, S. M.; Grätzel, M. Adv. Energy Mater. 2018, 8, No. 1800275.
- (10) Chen, W.; Wang, Y.; Pang, G.; Koh, C. W.; Djurišić, A. B.; Wu, Y.; Tu, B.; Liu, F.; Chen, R.; Woo, H. Y.; Guo, X.; He, Z. *Adv. Funct. Mater.* **2019**, 29, No. 1808855.
- (11) Jiang, Y.; Wang, C.; Rogers, C. R.; Kodaimati, M. S.; Weiss, E. A. *Nat. Chem.* **2019**, *11*, 1034–1040.
- (12) Li, Z.; Ji, S.; Liu, Y.; Cao, X.; Tian, S.; Chen, Y.; Niu, Z.; Li, Y. Chem. Rev. 2020, 120, 623-682.
- (13) Rust, M. J.; Bates, M.; Zhuang, X. Nat. Methods 2006, 3, 793-796.
- (14) Hell, S. W. Science 2007, 316, 1153-1158.
- (15) Wang, P.; Slipchenko, M. N.; Mitchell, J.; Yang, C.; Potma, E. O.; Xu, X.; Cheng, J.-X. *Nat. Photonics* **2013**, *7*, 449–453.
- (16) Hofmann, M.; Eggeling, C.; Jakobs, S.; Hell, S. W. Proc. Natl. Acad. Sci. U.S.A. 2005, 102, 17565–17569.
- (17) Binnig, G.; Rohrer, H. Surf. Sci. 1983, 126, 236-244.
- (18) Giessibl, F. J. Rev. Mod. Phys. 2003, 75, 949-983.
- (19) Kravtsov, V.; Ulbricht, R.; Atkin, J. M.; Raschke, M. B. Nat. Nanotechnol. 2016, 11, 459-464.
- (20) Centrone, A. Annu. Rev. Anal. Chem. 2015, 8, 101-126.
- (21) Knoll, B.; Keilmann, F. Nature 1999, 399, 134-137.
- (22) Dazzi, A.; Prazeres, R.; Glotin, F.; Ortega, J. M. Opt. Lett. 2005, 30, 2388.
- (23) Dazzi, A.; Glotin, F.; Carminati, R. J. Appl. Phys. 2010, 107, No. 124519.
- (24) Lahiri, B.; Holland, G.; Centrone, A. Small 2013, 9, 439-445.
- (25) Chae, J.; An, S.; Ramer, G.; Stavila, V.; Holland, G.; Yoon, Y.; Talin, A. A.; Allendorf, M.; Aksyuk, V. A.; Centrone, A. *Nano Lett.* **2017**, *17*, 5587–5594.
- (26) Katzenmeyer, A. M.; Holland, G.; Kjoller, K.; Centrone, A. Anal. Chem. 2015, 87, 3154–3159.
- (27) Dong, R.; Fang, Y.; Chae, J.; Dai, J.; Xiao, Z.; Dong, Q.; Yuan, Y.; Centrone, A.; Zeng, X. C.; Huang, J. *Adv. Mater.* **2015**, *27*, 1912–1918.
- (28) Katzenmeyer, A. M.; Canivet, J.; Holland, G.; Farrusseng, D.; Centrone, A. *Angew. Chem. Int. Ed.* **2014**, *53*, 2852–2856.
- (29) Kennedy, E.; Al-Majmaie, R.; Al-Rubeai, M.; Zerulla, D.; Rice, J. H. J. Biophotonics **2015**, *8*, 133–141.
- (30) Schwartz, J. J.; Jakob, D. S.; Centrone, A. Chem. Soc. Rev. 2022, 51, 5248-5267.
- (31) Kurouski, D.; Dazzi, A.; Zenobi, R.; Centrone, A. Chem. Soc. Rev. **2020**, 49, 3315–3347.
- (32) Huth, F.; Govyadinov, A.; Amarie, S.; Nuansing, W.; Keilmann, F.; Hillenbrand, R. *Nano Lett.* **2012**, *12*, 3973–3978.
- (33) Frogley, M. D.; Lekkas, I.; Kelley, C. S.; Cinque, G. Infrared Phys. Technol. 2020, 105, No. 103238.
- (34) Chan, K. L. A.; Lekkas, I.; Frogley, M. D.; Cinque, G.; Altharawi, A.; Bello, G.; Dailey, L. A. *Anal. Chem.* **2020**, 92, 8097–8107.
- (35) Jones, A. C.; Kearns, N. M.; Bohlmann Kunz, M.; Flach, J. T.; Zanni, M. T. J. Phys. Chem. A 2019, 123, 10824-10836.
- (36) Jones, A. C.; Bohlmann Kunz, M.; Tigges-Green, I.; Zanni, M. T. *Opt. Express* **2019**, *27*, 37236–37247.
- (37) Hamm, P.; Zanni, M. T. Concepts and Methods of 2d Infrared Spectroscopy; Cambridge University Press: Cambridge; New York, 2011.
- (38) Shim, S.-H.; Zanni, M. T. Phys. Chem. Chem. Phys. 2009, 11, 748-761.
- (39) Park, B.; Lee, S.; Kwon, J.; Kim, W.; Jung, S.; Kim, C. Sci. Rep. **2021**, 11, No. 17097.

- (40) Armstrong, Z. T.; Kunz, M. B.; Jones, A. C.; Zanni, M. T. J. Phys. Chem. C 2020, 124, 15123–15131.
- (41) Dazzi, A.; Prater, C. B. Chem. Rev. 2017, 117, 5146-5173.
- (42) Kim, B.; Khan, R. M.; Fast, A.; Fishman, D. A.; Potma, E. O. J. Phys. Chem. C 2020, 124, 11694–11700.